Supplemental Material: Spin-orbit-lattice entangled state in A_2MgReO_6 (A = Ca, Sr, Ba) revealed by resonant inelastic X-ray scattering

Felix I. Frontini,[1,*] Graham H.J. Johnstone,[1] Naoya Iwahara,[2] Pritam Bhattacharyya,[3] Nikolay A. Bogdanov,[4] Liviu Hozoi,[3] Mary H. Upton,[5] Diego M. Casa,[5] Daigorou Hirai,[6] and Young-June Kim[1,†]

[1] *Physics Department, University of Toronto, 60 St. George Street, Toronto, ON, M5S 1A7*
[2] *Graduate School of Engineering, Chiba University, 1-33 Yayoi-cho, Inage-ku, Chiba-shi, Chiba 263-8522, Japan*
[3] *Institute for Theoretical Solid State Physics, Leibniz IFW Dresden, Helmholtzstraße 20, 01069 Dresden, Germany*
[4] *Max Planck Institute for Solid State Research, Heisenbergstraße 1, 70569 Stuttgart, Germany*
[5] *Advanced Photon Source, Argonne National Laboratory, 9700 S. Cass Avenue, Lemont, IL 60439*
[6] *Department of Materials, Physics and Energy Engineering, Nagoya University, Furo-cho, Chikusa-ku, Nagoya, 464-8601, Japan*

(Dated: May 31, 2024)

I. VIBRONIC RIXS MODEL

A. Theory

The model Hamiltonian for a single Re site consists of spin-orbit and dynamic Jahn-Teller terms:

$$\hat{H} = \hat{H}_{\mathrm{SO}} + \hat{H}_{\mathrm{JT}}, \tag{1}$$

$$\hat{H}_{\mathrm{SO}} = \lambda \hat{\boldsymbol{l}} \cdot \hat{\boldsymbol{s}}, \tag{2}$$

$$\hat{H}_{\mathrm{JT}} = \sum_{\gamma=u,v} \frac{\hbar\omega}{2}\left(\hat{p}_\gamma^2 + \hat{q}_\gamma^2\right) + \hbar\omega g\left[\left(-\frac{1}{2}\hat{q}_u + \frac{\sqrt{3}}{2}\hat{q}_v\right)\hat{P}_{yz} + \left(-\frac{1}{2}\hat{q}_u - \frac{\sqrt{3}}{2}\hat{q}_v\right)\hat{P}_{zx} + \hat{q}_v\hat{P}_{xy}\right]. \tag{3}$$

Here, $\hat{\boldsymbol{l}}$ is the $\tilde{l} = 1$ effective orbital angular momentum operator for the t_{2g} orbitals [1], $\hat{\boldsymbol{s}}$ the spin angular momentum operator, λ the spin-orbit coupling parameter, $\hat{q}_\gamma$ the dimensionless normal coordinates for the Jahn-Teller active E_g modes [$\gamma = u\ (2z^2 - x^2 - y^2), v\ (x^2 - y^2)$] $\hat{p}_\gamma$ the conjugate momenta, $\hat{P}_\gamma$ ($\gamma = yz, zx, xy$) the projection operator into the $t_{2g}\gamma$ orbital, g the dimensionless vibronic coupling parameter, and ω the frequency for the Jahn-Teller active mode.

The energy scale of the spin-orbit coupling is one order of magnitude larger than that of the vibronic coupling. The spin-orbit coupling parameter λ of Re ion would be about 0.3-0.4 eV. The energy scale of the vibronic coupling $\hbar\omega g \approx 0.05$-$0.10$ eV because $g \approx 1$ for similar $5d^1$ compounds [2] and the frequency $\omega = 0.067$ eV according to the Raman scattering spectra for Ba_2MgWO_6 [3].

The energy eigenstates of the model Hamiltonian have the quantum entangled form of spin, orbit, and lattice degrees of freedom. Without the vibronic coupling ($g = 0$), the energy eigenstates are the direct products of the spin-orbit multiplet states and the vibrational states:

$$|J, M_J\rangle \otimes |n_u, n_v\rangle. \tag{4}$$

Here, $|J, M_J\rangle$ are the spin-orbit coupled states, and $|n_u, n_v\rangle$ ($n_u, n_v = 0, 1, 2, ...$) are the energy eigenstates of the harmonic oscillation Hamiltonian. Turning on the vibornic coupling, the low-energy states (vibronic states) of the system $\hat{H}$ take the form of linear combinations of product states (4):

$$|\nu\rangle = \sum_{J,M_J} |J, M_J\rangle \otimes |\chi_{J,M_J}\rangle, \tag{5}$$

$$|\chi_{J,M_J}\rangle = \sum_{n_u,n_v} |n_u, n_v\rangle c_{n_u n_v; J, M_J}. \tag{6}$$

* felix.frontini@mail.utoronto.ca
† youngjune.kim@utoronto.ca

Here, $|\nu\rangle$ indicates the vibronic states (energy eigenstates of $\hat{H}$), $|\chi\rangle$ involves the information of the lattice degrees of freedom, and $c_{n_u n_v;J,M_J}$ are coefficients. The energy levels E_ν (vibronic levels) are either four-fold degenerate (Γ_8) or doubly degenerate (Γ_6 or Γ_7). We calculated the cross-section of Re L_3-edge RIXS process between vibronic states. See for the detailed description Refs. [4, 5]. We assume that the present RIXS process is

$$2p^6 t_{2g}^1 + \hbar\omega_k \rightarrow 2p^5 t_{2g}^2 \rightarrow 2p^6 t_{2g}^1 + \hbar\omega_{k'}.$$

We only consider the dipole interaction between the light and the electron. The cross-section is

$$I \propto \sum_\nu \rho_\nu \frac{\omega_{k'}}{\omega_k} \left| \langle \nu'; \boldsymbol{k}'\lambda' | \hat{D}_{\boldsymbol{k}'\lambda'} \hat{G}(z_k) \hat{D}_{\boldsymbol{k}\lambda} | \nu; \boldsymbol{k}\lambda \rangle \right|^2 \times \delta(E_\nu + \hbar\omega_k - E_{\nu'} - \hbar\omega_{k'}), \tag{7}$$

using the Kramers-Heisenberg formula [6]. Here $\hat{D}_{\boldsymbol{k}\lambda}$ is the dipole moment operator projected along the direction of the photon polarization $\boldsymbol{k}\lambda$, and $\hat{G}(z_k)$ is the propagator of the intermediate $(2p)^5(5d)^2$ excitonic states. The propagator reduces to a constant $\bar{G}$ times the projector into the core-hole states within the fast collision approximation [7, 8]: $\bar{G} \approx 1/(i\Gamma)$ where Γ for Re would be about 4-5 eV [9]. We used the experimental scattering geometry: the incident and scattered photons are π-polarized, and the momentum transfers $\boldsymbol{k}' - \boldsymbol{k} = \boldsymbol{q}$ are as follows:

- $\boldsymbol{q} = (5.4, 5.4, 6)^T$ at 6 K and $(5.6, 5.6, 5.6)^T$ at 300 K for Ba_2MgReO_6,
- $\boldsymbol{2\theta} = 90°$ for Ca_2MgReO_6
- $\boldsymbol{q} = (4.24, 4.24, 4.47)^T$ at 11 K for Sr_2MgReO_6,

within the cubic coordinate system. To reproduce the shape of RIXS spectrum, we convoluted Eq. (7) with Gaussian function,

$$G(x) = \frac{1}{\sqrt{2\pi}\sigma} \exp\left[-\frac{1}{2} \left(\frac{x}{\sigma} \right)^2 \right]. \tag{8}$$

Here σ is the line widths of the Gaussian function.

B. Results and discussions

We reproduced the $j = 1/2$ part of the RIXS spectra at low temperature and then raised the temperature. We assumed that the systems are octahedral. We included the variation of the frequency with respect to temperature (Appendix I D):

$$\omega(T) = \omega_0 + cT. \tag{9}$$

We estimated the ω at 6 K using the Raman scattering data of Ba_2MgWO_6 [3]. We also modified the vibronic coupling g by varying ω while keeping V constant:

$$g = \frac{V}{\sqrt{\hbar\omega(T)^3}}. \tag{10}$$

TABLE I. Interaction parameters and the widths for the calculations of the RIXS spectra (in eV).

	Ba_2MgReO_6		Ca_2MgReO_6		Sr_2MgReO_6
	6 K	300 K	11 K	300 K	11 K
λ	0.311	0.311	0.347	0.347	0.337
$\frac{3}{2}\lambda$	0.467	0.467	0.515	0.515	0.505
g	1.325	1.350	1.250	1.275	1.275
ω	0.06733	0.06646	0.06733	0.06646	0.06733
σ (Gaussian)	0.042	0.047	0.028	0.031	0.031

C. Vibronic coupling

We explain the vibronic coupling (simple case). The vibronic coupling is the Taylor expansion of $\Delta\hat{H}_{\rm e} = \hat{H}_{\rm e}(Q) - \hat{H}_{\rm e}(0)$ with respect to the deformation from the reference geometry (Herzberg-Teller expansion) [10]:

$$\Delta\hat{H}_{\rm e} = \sum_{\alpha}\left(\frac{\partial\hat{H}_{\rm e}}{\partial Q_\alpha}\right)_{Q=0}\hat{Q}_\alpha + \sum_{\alpha\beta}\frac{1}{2!}\left(\frac{\partial^2\hat{H}_{\rm e}}{\partial Q_\alpha\partial Q_\beta}\right)_{Q=0}\hat{Q}_\alpha\hat{Q}_\beta + \cdots . \tag{11}$$

Here $\hat{H}_{\rm e}$ the electronic Hamiltonian, and Q the mass-weighted normal coordinates [see e.g. §10.1 in Ref. [11]]. At $Q = 0$, the system takes a reference structure: In the present case, we took the equilibrium octahedral structure as the reference. In this subsection, for simplicity, we consider that both the electronic and vibrational mode are nondegenerate.

We define vibronic coupling V by the gradient of the electronic energy, $U = \langle\Psi|\,\hat{H}_{\rm e}\,|\Psi\rangle$:

$$V = \left(\frac{\partial U(Q)}{\partial Q}\right)_{Q=0}, \tag{12}$$

by using the Hellmann-Feynman theorem. Similarly, we define the frequency by

$$\omega^2 = \left(\frac{\partial^2 U(Q)}{\partial Q^2}\right)_{Q=0}. \tag{13}$$

The description of V and ω becomes slightly complicated in the case of Jahn-Teller systems.

We define the dimensionless quantities as follows:

$$g = \frac{V}{\sqrt{\hbar\omega^3}}, \quad Q = \sqrt{\frac{\hbar}{\omega}}q. \tag{14}$$

D. Temperature dependence of the frequency

We estimated the temperature dependence of the frequency ω from the Raman data. We digitized the frequency for the E_g mode (Fig. 6 in Ref. [3]) and did a least squares fit to the linear function,

$$\omega(T) = \omega_0 + cT. \tag{15}$$

See for the fitting Fig. 1 We obtained $\omega_0 = 543.2$ cm^{-1} (67.34 meV) and $c = -0.024$ cm^{-1}/K (-0.0030 meV/K). At $T = 6$ K, $\omega = 543.0$ cm^{-1} (67.33 meV), which is about 1.3 % larger than the frequency (536 cm^{-1}, 66.46 meV) at 300 K.

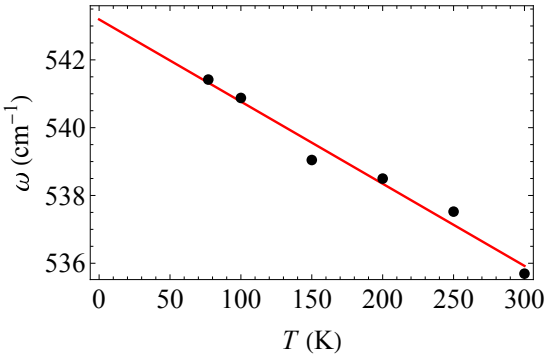

FIG. 1. Frequency with respect to temperature. We took the experimental data (the black points) from Ref. [3]. The red solid line indicates the linear function.

E. Treatment of static distortions

We estimated the effect of static distortions using via a tetragonal ligand field, which modifies the single Re site hamiltonian as follows:

$$\hat{H} = \hat{H}_{\mathrm{SO}} + \hat{H}_{\mathrm{JT}} + \hat{H}_{\mathrm{LF}}, \tag{16}$$

$$\hat{H}_{\mathrm{LF}} = \Delta \left(-\frac{1}{2}\hat{P}_{yz} - \frac{1}{2}\hat{P}_{zx} + \hat{P}_{xy} \right), \tag{17}$$

Here, $\hat{H}_{\mathrm{SO}}$ and $\hat{H}_{\mathrm{JT}}$ are unchanged and Δ represents the orbital splitting originating from static tetragonal distortion. This new Hamiltonian is applied to the most distorted system, Ca_2MgReO_6, in order to estimate the impact of static distortions in the most significant case. A ligand field of $\Delta = 0.07$ meV is applied based on our MRCI+SOC calculations, see section II. The RIXS spectra at 11 K with and without static distortions accounted for are shown in Fig.I E

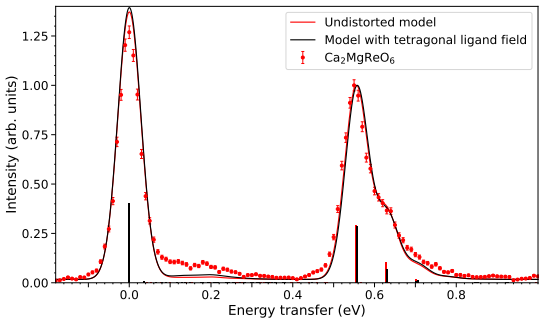

FIG. 2. Ca_2MgReO_6 RIXS spectra below 1 eV overlayed with undistorted vibronic RIXS model (red) and tetragonally distorted vibronic RIXS model

This treatment of static distortions results in a largely unchanged RIXS spectrum and gives a reduced SOC of 326 meV, down from 347 meV in the absence of distortion. This value is much closer to that of Ba_2MgReO_6 and indicates that the addition of a Δ_3 gap succeeds fairly well in its mission of separating the effect of static distortions from that of spin-orbit and vibronic couplings. Additionally, the vibronic coupling constant is reduced from g=1.25 to g=1.175, strengthening the notion that the originally observed trend could reflect the corresponding increase in static distortions. However, the reduction is fairly small and it remains the case that, overall, the vibronic coupling constant is remarkably robust against static distortions as far as can be quantitatively determined. This simple treatment provides a qualitative picture that highlights the coexistence of the static and dynamic JT effects.

II. MRCI+SOC QUANTUM CHEMISTRY CALCULATIONS

All quantum chemical computations were carried out using the MOLPRO suite of programs [12]. For each type of embedded cluster, the crystalline environment was modeled as a large array of point charges which reproduces the crystalline Madelung field within the cluster volume; we employed the EWALD program [13, 14] to generate the point-charge embeddings. To understand the Re-site 5*d* electronic structure, a cluster consisting of one 'central' ReO_6 octahedron, the six adjacent Mg cations, and eight Ca/Sr/Ba nearest neighbors was considered. Crystal structures refined from powder X-ray diffraction spectra were used for each system. The room temperature (300 K) cubic, tetragonal, and monoclinic structures of Ba_2MgReO_6, Sr_2MgReO_6, and Ca_2MgReO_6 published in prior literature were utilized [15–17]. The crystal structure of Ba_2MgReO_6 at 93 K was refined using X-ray powder diffraction and validated by cross referencing our refinement at 300 K with the structure from literature. The quantum chemical study was initiated as complete active space self-consistent field (CASSCF) calculations [18, 19] with active orbital spaces containing the five 5*d* orbitals of the central Re ion. Post-CASSCF correlation computations were performed at the level of multireference configuration-interaction (MRCI) with single and double excitations [18, 20] out of the Re 5*d* and O 2*p* orbitals of the central ReO_6 octahedron. Spin-orbit couplings (SOCs) were accounted for following the procedure described in Ref. [21]. For the central Re ion energy-consistent relativistic pseudopotentials (ECP60MDF)

were employed [22] and Gaussian-type valence basis sets of effective quadruple-ζ quality (referred to as ECP60MDF-VTZ in the MOLPRO library), whereas we used all-electron triple-ζ basis sets for the O ligands of the central ReO_6 octahedron [23]. Large-core pseudopotentials were adopted for the adjacent six Mg (ECP10SDF) [24] and eight Ca/Sr/Ba (ECP18SDF/ECP36SDF/ECP54SDF) [24] cations, along with (4s4p)/[1s1p] valence basis sets.

The basic Re^{6+} $5d^1$ multiplet structures obtained by spin-orbit MRCI (MRCI+SOC) for Ba_2MgReO_6, Sr_2MgReO_6, and Ca_2MgReO_6 are depicted in Table II. For the latter two compounds, due to distortions that yield point-group symmetry lower than cubic, the degeneracy of the spin-orbit j=3/2 t_{2g}^1 and of the e_g^1 states is lifted. While the noncubic splittings within the e_g sector (also referred to as δ_1 parameters) lie in the region of 0.2–0.3 eV (see Table II), those within the t_{2g} components (Δ_3), as computed by CASSCF (configuration-interaction effects and SOCs excluded), amount to 0.07 (Sr_2MgReO_6) and 0.11 (Ca_2MgReO_6) eV (not shown in Table II).

It is seen that our frozen-lattice MRCI+SOC calculations overestimate, by ∼10%, peak positions in the RIXS spectra, for all three compounds. Yet, the overal trends seen in experiment are reproduced computationally: larger intra-t_{2g} and $t_{2g} \rightarrow e_g$ excitation energies for lighter alkaline-earth A ions. As concerns the slight overestimation of the $t_{2g} \rightarrow e_g$ excitation energies, it may indicate that our embeddings overestimate the ionic character of these compounds. The somewhat larger intra-t_{2g} excitation energies obtained computationally might indicate that the core potentials employed here overestimate SOC.

III. ADDITIONAL DATA

A. Expanded Spectra

1. Features

The RIXS spectra for all three members of the A_2MgReO_6 family are shown in Fig. 3 and display similar features. The RIXS spectra below 1 eV are shown in Fig. 3a), with all members displaying a low energy feature below ∼ 300 meV labelled 'A' and a feature labelled 'B' at ∼ 500-550 meV. It is observed that a systematic shift upwards in energy of the B feature occurs from Ba→Sr→Ca. The features above 1 eV are shown in Fig. 3b) and include a peak labelled

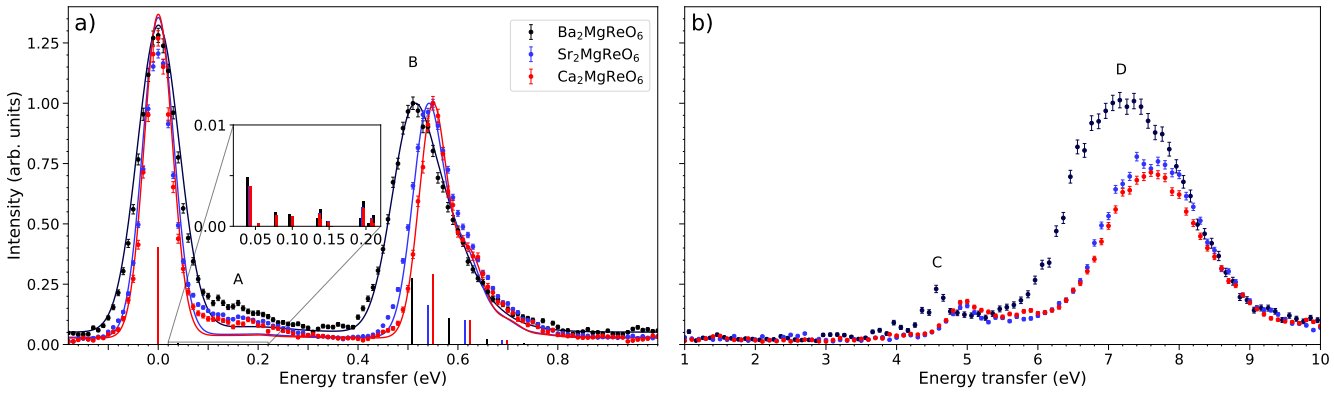

FIG. 3. a) A_2MgReO_6 (A = Ca, Sr, Ba) RIXS spectra up to 1 eV overlaid with vibronic RIXS model and b) RIXS spectra up to 10 eV.

'C' in situated between 4.5-5 eV common to all compounds. This feature is also observed to possess a systematic shift upwards in energy from Ba→Sr→Ca as observed with the B feature. The second high energy feature, labelled 'D' in Fig. 3b) is a large, broad feature near 7 eV in all compounds. The physical origin of features A, C and D is clarified by inspecting the incident energy dependence of the features, shown in Fig. 4 for Ba_2MgReO_6.

2. Incident Energy Dependence

As shown in Fig. 4, features A and B are observed to resonate at 10.532 keV, indicating a $2p^5t_{2g}^2$ intermediate state. Feature B is identified as the transition between the $j_{eff} = 3/2$ ground state and $j_{eff} = 1/2$ excited state of energy Δ_2 and is discussed at greater length in the main text. The exact nature of feature A is, however, unclear other than that it corresponds to some intra-$j_{eff} = 3/2$ excitation. Although it can be seen in Fig. 3a) that the A feature is not

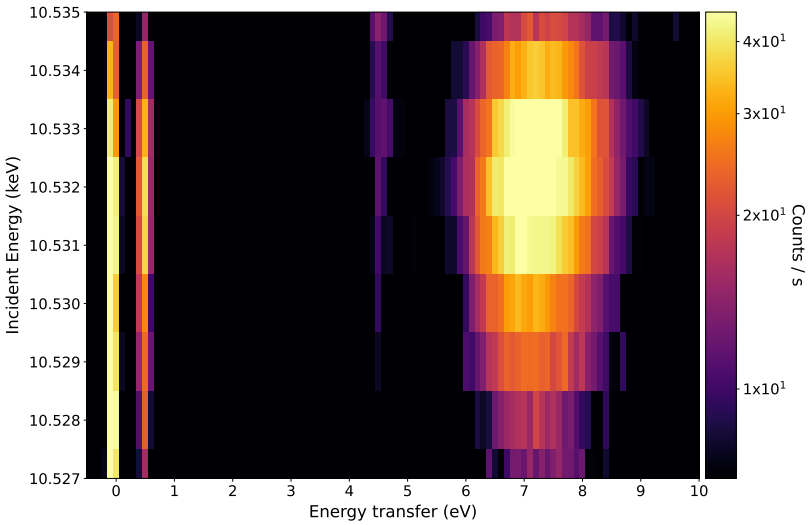

FIG. 4. Ba_2MgReO_6 RIXS spectrum up to 10 eV as a function of incident energy. The $j_{eff} = 1/2$ and charge-transfer excitations, near 0.5 and 7 eV respectively, can be seen to resonate at 10.532 keV while the e_g excitation near 4.5 eV resonates above 10.535 keV.

well reproduced by the excitation of vibronic modes at low energy, we note that the low energy vibronic modes exist at energies in reasonable agreement with the A feature. Thus, it is possible that the A feature represents low energy vibronic modes whose intensity is underestimated by our model. Complicating things, the feature does not show any noticeable broadening or shifting to higher energy at high temperature as observed with the vibronically coupled $j_{eff} = 1/2$ feature, though this effect may be very subtle considering the breadth and low intensity of the feature. Another possibility is that this feature instead represents crystal field splitting of the $j_{eff} = 3/2$ quartet of energy Δ_3 due to tetragonal or orthorhombic distortion of the octahedra. This is, however, implausible given that the feature occurs at a similar energy in each system regardless of the very different levels of octahedral distortion. In addition to this, it is shown in Table II that splitting of the $j_{eff} = 3/2$ quartet is not predicted to exceed 70 meV in any compound which stands in contrast to the higher energy of the A feature. The feature's temperature independence across the low temperature phase transitions of each system leads us to rule out its attribution to any kind of magnetic or quadrupolar collective excitation. A final possibility is that the feature represents non-local intra-$j_{eff} = 3/2$ charge excitations. This explanation does well in explaining the broadness and momentum independence of the feature by virtue of the broad continuum nature of electron-hole pair excitations. Countering this notion, we note that no distinct gap is observed below the A feature in any of the samples whereas the activation gap in Ba_2MgReO_6 is estimated to be $\sim$ 0.17-0.2 eV and is estimated to be of a similar magnitude in related rhenate and osmate DPs [15, 25–27]. If the A feature does represent intraband charge excitations, then, we must conclude that the activation gap in Ba_2MgReO_6 has been significantly overestimated. Thus the origin of the feature remains somewhat obscure other than to say it corresponds to some intra-$j_{eff} = 3/2$ excitation with plausible explanations found in intraband charge excitations and in vibronic contributions underestimated by our model. Understanding of this feature would be greatly aided by RIXS studies with greater resolution which may reveal whether the excitation is gapped, indicating a likely charge excitation origin, or gapless, indicating a likely vibronic origin.

Upon inspection of the incident energy dependence of the high energy features, it is shown that feature C resonates at higher energy beyond our limit whereas feature D resonates at 10.532 keV, the same energy as the $j_{eff} = 1/2$ feature. This indicates that the intermediate state of the D feature is the same as that of the $j_{eff} = 1/2$ feature, namely $2p^5t_{2g}^2$. It follows that the D feature represents charge-transfer excitations due to $2p - 5d$ hybridization. This value is also in line with energy levels of charge-transfer excitations found in other $5d$ DPs [28]. Conversely, the fact that the C feature resonates at higher incident X-ray energy indicates that the intermediate state lies at higher energy, namely it is $2p^5t_{2g}^1e_g^1$. Thus feature C corresponds to a $j_{eff} = 3/2 \rightarrow e_g$ transition of energy Δ_1. The crystal field splitting is thus on the order of 5 eV which is once again in line with that found in other $5d$ DPs [28].

TABLE II. Re^{6+} $5d^1$ splittings in the three A_2MgReO_6 (A = Ca, Sr, Ba) compounds at select temperatures, relative energies in eV. Calculated Sr_2MgReO_6 and Ca_2MgReO_6 $j_{eff} = 3/2$ and e_g states are split due to their distorted octahedra. The last column gives the average $Re - O$ bond length for each compound in angstrom [15–17].

	$\Delta_2^{exp.}$	$\Delta_1^{exp.}$	$\Delta_3^{calc.}$	$\Delta_2^{calc.}$	$\Delta_1^{calc.}$	$Re - O$ (Å)
Ca_2MgReO_6 300 K	0.555(5)	-	0.07	0.61	5.34, 6.14	1.928
11 K	0.545(5)	4.95(5)	-	-	-	-
Sr_2MgReO_6 300 K	-	-	0.05	0.60	5.46, 5.69	1.948
11 K	0.535(5)	4.91(5)	-	-	-	-
Ba_2MgReO_6 300 K	0.52(2)	4.56(5)	0	0.57	5.32	1.961
93 K	-	-	0	0.57	5.35	1.957
6 K	0.50(1)	-	-	-	-	-

3. A_2MgReO_6 A *Site Dependence*

As previously discussed, a systematic energy shift is observed in both the $j_{eff} = 1/2$ levels and the e_g levels as the A_2MgReO_6 A site is substituted from Ba → Sr → Ca. This information as well as MRCI+SOC quantum chemistry calculation results are summarized in Table II. The former shift can be understood by examining the Re ion crystal field environment in each member of the series. In the case of a cubic crystal field the $5d$ manifold is split into the t_{2g} and e_g manifolds before being further split into the $j_{eff} = 3/2$ quartet and $j_{eff} = 1/2$ doublet by spin-orbit coupling. In this case the $j_{eff} = 3/2 \rightarrow 1/2$ excitation is of energy $\Delta_2 = 3\lambda/2$, however, this energy is increased if a distortion is induced in the crystal field. Whilst Ba_2MgReO_6 displays a slight tetragonal distortion of the ReO_6 octahedra below T_q, this distortion is much smaller than the innate distortion of the ReO_6 octahedra in Sr_2MgReO_6, which is in turn smaller than the distortion of the ReO_6 octahedra in Ca_2MgReO_6 [16, 17, 29]. It should be noted that in the case of Ca_2MgReO_6 the distortion is not simply tetragonal but is in fact orthorhombic. Nevertheless, this distortion of the octahedral crystal field from the cubic limit will result in a splitting of the $j_{eff} = 3/2$ quartet and correspondingly in an increase of the $j_{eff} = 1/2$ level. The observed systematic increase in the $j_{eff} = 1/2$ peak energy across the series is thus consistent with an analysis of the deviation of the Re site crystal field from the cubic limit. This interpretation is also supported by MRCI+SOC calculations which replicate both this systematic trend as well as the relative shift in peak position, as shown in Table II. Specifically, the MRCI+SOC calculations replicate a ~ 40 meV shift in the $j_{eff} = 1/2$ peak position from Ba → Sr and a ~ 10 meV shift from Sr → Ca. The calculations are noted to overestimate the experimentally determined peak positions by about 10% as discussed in Section II.

The latter shift of the e_g levels can also be understood by inspecting the specifics of the Re site crystal field, this time with regards to its magnitude as opposed to its symmetry. The magnitude of the crystal field is, necessarily, dependent on the proximity of the ligand oxygen ions, with the field magnitude increasing as the ligand oxygens are brought closer to the central Re site. The systematic shift is then elucidated by inspecting the average $Re - O$ bond length of each compound, shown in Table II. It is observed that the average $Re - O$ bond length shrinks from Ba → Sr → Ca, consistent with the observed energetic shift of the e_g levels. There are, however, two factors which complicate this simple picture. First, we must address the fact that we expect the e_g levels also to be split by distortion of the ReO_6 octahedra. At room temperature, this splitting is predicted by MRCI+SOC calculations to be ~ 0.2 eV in Sr_2MgReO_6 and ~ 0.8 eV in Ca_2MgReO_6. Unfortunately, due to the proximity of the e_g feature to the charge-transfer feature we were unable to resolve any splitting of the e_g levels. We can, however, make some inferences on the impact of e_g splitting. On the one hand, the average $Re - O$ bond lengths of Sr_2MgReO_6 and Ca_2MgReO_6 necessitate that an unsplit Ca_2MgReO_6 e_g level be located significantly higher than that of Sr_2MgReO_6, whereas in reality the resolved e_g levels of the two compounds lie within each others' uncertainty. This suggests that there is indeed significant splitting of the Ca_2MgReO_6 e_g levels. On the other hand, we can decidedly rule out that the lowest Ca_2MgReO_6 e_g level lies 100 meV below the lowest Sr_2MgReO_6 level as predicted by MRCI+SOC, which suggests that the predicted e_g level splitting is overestimated. We note that as with the $j_{eff} = 1/2$ levels the calculated e_g levels are overestimated by about 10% but do faithfully replicate an overall upwards energetic shift of the e_g levels from Ba → Sr → Ca. Secondly, the question of temperature dependence must be addressed since the Ba_2MgReO_6 RIXS spectrum up to 10 eV was collected at 300 K whereas the Sr_2MgReO_6 and Ca_2MgReO_6 spectra were collected at 11 K. To help answer this question, powder X-ray diffraction structural refinements of Ba_2MgReO_6 were carried out at room temperature and at 93 K, with the resulting structures used to perform MRCI+SOC calculations. Our refinements show that the lattice contraction between 300 K and 93 K leads to a contraction of the $Re - O$ bond length from ~ 1.961 Å to 1.957 Å and, correspondingly, to an increase in the e_g level energy from 5.32 eV to 5.35 eV. Given that a change of 30 meV is estimated to occur over > 200 K we anticipate the difference between 11 K and 300 K to be of the same order of magnitude. Such a change in the Ba_2MgReO_6 e_g levels would be noticeable but would

not change the analysis of the systematics in play.

Another, similarly rooted interpretation of the larger Δ_1 energies from Ba→Sr→Ca examines the effect of the smaller lattice constants for lighter A cations: having the adjacent B′ Re^{6+} species closer by (for reduced lattice parameters) stabilizes the $5d$ t_{2g} levels (with respect to the e_g counterparts), since the lobes of each t_{2g} orbital point toward four of the nearest Re^{6+} neighbors. This effect is even stronger in Os^{7+} $5d^1$ double perovskites [30] since the charge imbalance between the B and B′ varieties (1+ vs 7+ for divalent A cations) is even more pronounced.

B. Ba_2MgReO_6 Momentum Dependence

Momentum dependence of the features below 1 eV was investigated in Ba_2MgReO_6 near the magnetic ordering wavevector $q_m = G + (1\ 0\ 0)_c$ below T_m and in between T_m and T_q. To minimize thomson scattering, the magnetic zone center $q_m = (6\ 5\ 5)_c$ was chosen for its proximity to $2\theta = 90°$. No features were observed to be dispersive within the resolution limits and no momentum dependence was observed other than an expected decrease in magnetic Bragg reflection intensity in the elastic channel, shown in Fig. 5. We note that recent theoretical work predicts non-trivial momentum dependence of multi-phonon excitations in RIXS and, while our measurements are unable to resolve such behaviour, the magnitude of the predicted dispersion is much lower than our instrumental resolution and as such may be obscured [31]. The magnetic Bragg peak is found to be remarkably broad in momentum space, with a FWHM

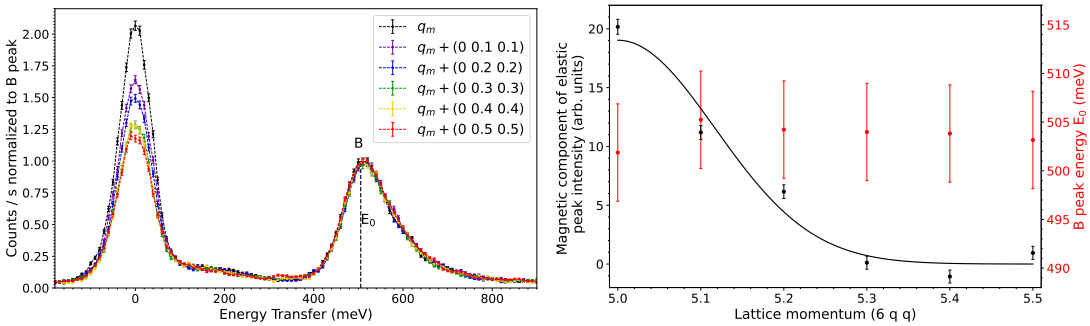

FIG. 5. Left: Momentum dependence of the Ba_2MgReO_6 RIXS spectrum below 1 eV near $q_m = (6\ 5\ 5)$. Right: Extracted momentum dependence of the magnetic Bragg reflection intensity (black) and B feature energy (red)

.

estimated of $\sim 0.4b_c$, where b_c is the magnitude of the cubic unit cell reciprocal space basis vector.

C. Sr_2MgReO_6 Temperature Dependence

Temperature dependence of the Sr_2MgReO_6 RIXS spectrum below 1 eV was studied above and below the magnetic ordering phase transition temperature of $T_N = 55$ K. RIXS spectrum were collected at T = 70 K and 11 K, shown in Fig.6. No temperature dependence is observed in the RIXS spectrum across T_N, indicating that none of the observed features correspond to collective magnetic excitations, in particular the broad feature present below 300 meV.

D. Expanded Ba_2MgReO_6 and Ca_2MgReO_6 Temperature Dependence

The temperature dependence of the low energy Ba_2MgReO_6 and Ca_2MgReO_6 features are shown in Fig.7 in the expanded energy range that includes the elastic line and A feature.

ACKNOWLEDGMENTS

Work at the University of Toronto was supported by the Natural Sciences and Engineering Research Council (NSERC) of Canada through the Discovery Grant No. RGPIN-2019-06449 and the Alliance International Catalyst Quantum Grant No. ALLRP 576422 - 22, Canada Foundation for Innovation, and Ontario Research Fund. This work was partly supported by Grant-in-Aid for Scientific Research (Grant No. 22K03507 and 20H01858) from the Japan

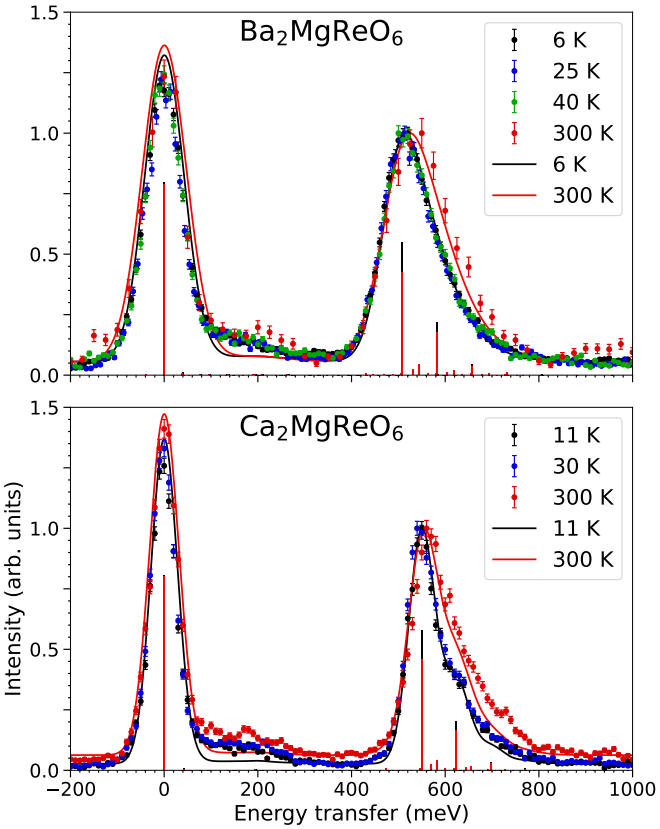

FIG. 6. Temperature dependence of the Sr_2MgReO_6 RIXS spectrum below 1 eV above and below $T_N = 55$ K.

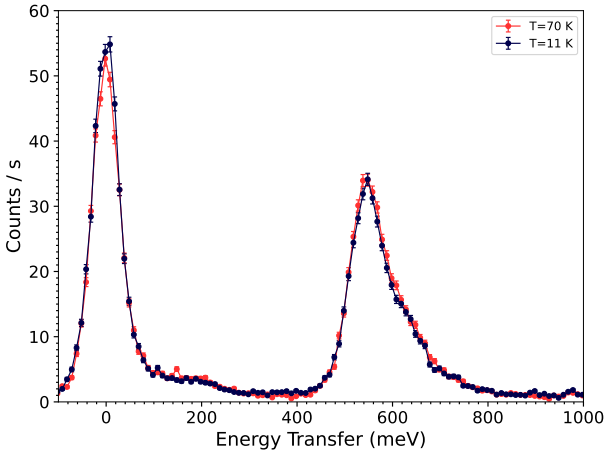

FIG. 7. Temperature dependence of the Ba_2MgReO_6 and Ca_2MgReO_6 RIXS spectra below 1 eV.

Society for the Promotion of Science, JSPS Bilateral Program (Grant No. JPJSBP120239915) and the Iketani Science and Technology Foundation. P. B. and L. H. acknowledge financial support from the German Research Foundation

(Deutsche Forschungsgemeinschaft, DFG), project 441216021, and technical assistance from U. Nitzsche.

---

[1] S. Sugano, Y. Tanabe, and H. Kamimura, *Multiplets of Transition-Metal Ions in Crystals* (Academic Press, New York, 1970).
[2] N. Iwahara, V. Vieru, and L. F. Chibotaru, Phys. Rev. B **98**, 075138 (2018).
[3] J. Pásztorová, W. H. Bi, R. Gaal, K. Krämer, I. Živkoviá, and H. M. Rønnow, J. Solid State Chem. **326**, 124184 (2023).
[4] N. Iwahara and S. Shikano, Phys. Rev. Res. **5**, 023051 (2023).
[5] N. Iwahara and W. Furukawa, Phys. Rev. B **108**, 075136 (2023).
[6] J. J. Sakurai, *Advanced Quantum Mechanics* (Addison-Wesley, Massachusetts, 1967).
[7] J. Luo, G. T. Trammell, and J. P. Hannon, Phys. Rev. Lett. **71**, 287 (1993).
[8] M. van Veenendaal, Phys. Rev. Lett. **96**, 117404 (2006).
[9] J. P. Clancy, N. Chen, C. Y. Kim, W. F. Chen, K. W. Plumb, B. C. Jeon, T. W. Noh, and Y.-J. Kim, Phys. Rev. B **86**, 195131 (2012).
[10] I. B. Bersuker and V. Z. Polinger, *Vibronic Interactions in Molecules and Crystals* (Springer-Verlag, Berlin and Heidelberg, 1989).
[11] T. Inui, Y. Tanabe, and Y. Onodera, *Group Theory and Its Applications in Physics* (Springer-Verlag, Berlin and Heidelberg, 1990).
[12] H.-J. Werner, P. J. Knowles, G. Knizia, F. R. Manby, and M. Schütz, WIREs Comput. Mol. Sci. **2**, 242 (2012).
[13] M. Klintenberg, S. Derenzo, and M. Weber, Comp. Phys. Commun. **131**, 120 (2000).
[14] S. E. Derenzo, M. K. Klintenberg, and M. J. Weber, J. Chem. Phys. **112**, 2074 (2000).
[15] D. Hirai and Z. Hiroi, Journal of the Physical Society of Japan **88**, 064712 (2019), https://doi.org/10.7566/JPSJ.88.064712.
[16] S. Gao, D. Hirai, H. Sagayama, H. Ohsumi, Z. Hiroi, and T.-h. Arima, Phys. Rev. B **101**, 220412 (2020).
[17] K. G. Bramnik, H. Ehrenberg, J. K. Dehn, and H. Fuess, Solid State Sciences **5**, 235 (2003), dedicated to Sten Andersson for his scientific contribution to Solid State and Structural Chemistry.
[18] T. Helgaker, P. Jørgensen, and J. Olsen, *Molecular Electronic Structure Theory* (John Wiley & Sons, Chichester, 2000).
[19] D. A. Kreplin, P. J. Knowles, and H.-J. Werner, J. Chem. Phys. **152**, 074102 (2020).
[20] P. J. Knowles and H.-J. Werner, Theor. Chim. Acta **84**, 95 (1992).
[21] A. Berning, M. Schweizer, H.-J. Werner, P. J. Knowles, and P. Palmieri, Mol. Phys. **98**, 1823 (2000).
[22] D. Figgen, K. A. Peterson, M. Dolg, and H. Stoll, J. Chem. Phys. **130**, 164108 (2009).
[23] T. H. Dunning, J. Chem. Phys. **90**, 1007 (1989).
[24] P. Fuentealba, L. von Szentpaly, H. Preuss, and H. Stoll, J. Phys. B: Atom. Mol. Phys. **18**, 1287 (1985).
[25] A. Mansouri Tehrani and N. A. Spaldin, Phys. Rev. Mater. **5**, 104410 (2021).
[26] B. Chamberland and G. Levasseur, Materials Research Bulletin **14**, 401 (1979).
[27] Y. Yuan, H. L. Feng, M. P. Ghimire, Y. Matsushita, Y. Tsujimoto, J. He, M. Tanaka, Y. Katsuya, and K. Yamaura, Inorganic Chemistry **54**, 3422 (2015), pMID: 25751088.
[28] B. Yuan, J. P. Clancy, A. M. Cook, C. M. Thompson, J. Greedan, G. Cao, B. C. Jeon, T. W. Noh, M. H. Upton, D. Casa, T. Gog, A. Paramekanti, and Y.-J. Kim, Phys. Rev. B **95**, 235114 (2017).
[29] D. Hirai, H. Sagayama, S. Gao, H. Ohsumi, G. Chen, T.-h. Arima, and Z. Hiroi, Phys. Rev. Res. **2**, 022063 (2020).
[30] L. Xu, N. A. Bogdanov, A. Princep, P. Fulde, J. Van Den Brink, and L. Hozoi, npj Quantum Materials **1**, 16029 (2016).
[31] K. Bieniasz, S. Johnston, and M. Berciu, Phys. Rev. B **105**, L180302 (2022).